Engineered synthesis of a novel bixbyite-structured high-entropy oxide
(Ce0.2Zr0.2Yb0.2Er0.2Gd0.2)2O3.4 as a stable and high-performing visible-light-active photocatalyst for

(Article begins on next page)

23 December 2025

Engineered synthesis of a novel bixbyite-structured high-entropy oxide $(Ce_{0.2}Zr_{0.2}Yb_{0.2}Er_{0.2}Gd_{0.2})_2O_{3.4}$ as a stable and high-performing visible-light-active photocatalyst for multifunctional pollutant degradation

Antonietta Mancuso [a], Katia Monzillo [a], Olga Sacco [b], Luca Spiridigliozzi [c,e,*],
Viviana Monfreda [c], Andrea Muscatello [d], Gianfranco Dell'Agli [c,e], Serena Esposito [d,**],
Vincenzo Vaiano [a]

[a] Department of Industrial Engineering, University of Salerno, Via Giovanni Paolo II 132, Fisciano, SA 84084, Italy
[b] Department of Chemistry and Biology "A.Zambelli", University of Salerno, Via Giovanni Paolo II 132, Fisciano, SA 84084, Italy
[c] Department of Civil and Mechanical Engineering, University of Cassino and Southern Lazio, Via G. Di Biasio 43, Cassino, FR 03043, Italy
[d] Department of Applied Science and Technology – INSTM Torino-Politecnico, Corso Duca degli Abruzzi, 24, Torino I-10129, Italy
[e] INSTM—National Interuniversity Consortium of Materials Science and Technology, Via G. Giusti 9, Florence 50121, Italy

ABSTRACT

This study presents a novel bixbyite-structured High Entropy Oxide (HEO), $(Ce_{0.2}Zr_{0.2}Yb_{0.2}Er_{0.2}Gd_{0.2})_2O_{3.4}$, synthesized through a straightforward and efficient co-precipitation method in a carbonate environment, as a next-generation photocatalyst for the removal of water pollutants under visible light irradiation. Calcination at 750 °C induced the formation of the entropy-stabilized HEO bixbyite single-phase as displayed by the diffraction pattern, characterized by a homogeneous distribution of the cations. The photocatalytic activity of $(Ce_{0.2}Zr_{0.2}Yb_{0.2}Er_{0.2}Gd_{0.2})_2O_{3.4}$ was assessed by examining the influence of pH, photocatalyst dosage and irradiation time on the degradation of methylene blue (MB). The optimal conditions for MB degradation were at pH = 11, with a catalyst dose of $1\,g\,L^{-1}$ and a reaction time of 180 min, achieving an MB degradation and mineralization efficiency of approximately 99 and 45 %, respectively. ANOVA analysis revealed that the MB removal efficiency was significantly influenced by the individual positive effects of irradiation time and pH, further confirming that the photocatalytic performance of $(Ce_{0.2}Zr_{0.2}Yb_{0.2}Er_{0.2}Gd_{0.2})_2O_{3.4}$ is strongly dependent on the adsorption of the target contaminant onto its surface. Analysis of the $(Ce_{0.2}Zr_{0.2}Yb_{0.2}Er_{0.2}Gd_{0.2})_2O_{3.4}$ band structure and reactive oxygen species involved in MB photodegradation (superoxide and hydroxyl radicals) suggested that this material acts as a direct band gap semiconductor. Moreover, the catalyst exhibited good stability and reusability over multiple cycles. The $(Ce_{0.2}Zr_{0.2}Yb_{0.2}Er_{0.2}Gd_{0.2})_2O_{3.4}$ photocatalyst was also capable of degrading gallic acid (a colorless pollutant), achieving near-complete degradation of this pollutant after 180 min of irradiation time without altering the solution pH and excluding possible photosensitization phenomena of $(Ce_{0.2}Zr_{0.2}Yb_{0.2}Er_{0.2}Gd_{0.2})_2O_{3.4}$ by MB molecules. These results highlight the potential of $(Ce_{0.2}Zr_{0.2}Yb_{0.2}Er_{0.2}Gd_{0.2})_2O_{3.4}$ as a highly efficient and durable visible light-driven photocatalyst for water purification, particularly in the removal of dye pollutants, but also in the degradation of other water contaminants like gallic acid at the spontaneous pH of the polluted water, offering a promising solution for multipurpose wastewater treatment.

1. Introduction

The stability of aquatic ecosystems is increasingly threatened by water contamination with pollutants [1–4]. One of the major global issues is the removal of organic pollutants from water sources [5]. A key group of contaminants in aquatic environments consists of dyes

generated during various industrial processes, such as textile production, dyeing, tanning, papermaking, and the manufacture of paints and pigments [6–8]. Methylene blue (MB), depicted in Fig. 1, is among the most commonly used dyes in these industries, and its growing concentration in water bodies poses significant risks to the health of plants and aquatic life [9]. Photocatalysis has garnered considerable interest as a promising method for a wide range of applications [10–12], including wastewater treatment [13–15]. Photocatalytic processes are triggered when a catalyst absorbs photons with energy that equals or exceeds the band gap energy (E_g) of the photocatalyst [16]. The absorption of photons by the catalyst induces the formation of electron-hole pairs on its surface. These electron-hole pairs can subsequently generate reactive oxygen species (ROS). These ROS possess the ability to degrade organic pollutants at ambient temperature and pressure. Among the diverse range of photocatalyst materials, titanium dioxide (TiO_2) and zinc oxide (ZnO) are widely employed for the photodegradation of organic dyes [17–21]. Nevertheless, these metal oxide semiconductors exhibit a substantial band gap, which restricts their photocatalytic activity to the UV region of the electromagnetic spectrum. This constraint renders them inefficient under solar illumination, as the UV portion constitutes only approximately 5 % of the total solar spectrum. Despite numerous efforts to improve their photocatalytic performance, such as doping with metallic or non-metallic elements during semiconductor preparation, TiO_2 and ZnO still face challenges in effectively harnessing visible light for photocatalysis [22–28]. On the other hand, high entropy oxides (HEOs) have been considered a new class of materials with a high degree of disorder, good chemical and thermal stability, catalytic activity, and durability. The concept of HEO photocatalysts emerged around 2015 as part of the broader discovery of high entropy materials (HEMs). Specifically, high entropy alloys were first proposed in 2004 [29], and the concept was extended to oxides around 2015 [30]. HEOs exhibit a complex crystal structure characterized by the random distribution of multiple metal cations (typically five or more) in near-equimolar ratios. This compositional heterogeneity results in intricate atomic interactions and a challenging structural landscape. In contrast to conventional metal oxides, the disordered arrangement of metal ions within the HEOs lattice leads to a significantly increased defect density. These defects, formulated as lattice distortions, can increase the mobility of oxygen in a metal oxide system, promoting the separation of photogenerated electron-hole pairs and reducing their recombination. The catalytic superiority of HEOs stems from the synergistic interplay of their multi-constituent lattice constraint and the oxygen deficiency induced by lattice strain [31].

Since Rost's publication [30], scientific interest in HEOs has grown exponentially, leading to the discovery of many differently structured systems, extending beyond the simple rock-salt structure up to much more complex crystal structures, including the bixbyite-like one [32–35]. This surge in global research interest is primarily due to HEOs promising, and often unexpected, technological properties [36,37]. In the context of photocatalysis, HEOs are studied for their electronic and structural potential to improve the efficiency of light-driven reactions, such as water splitting, pollutant degradation, and CO_2 reduction [38–40]. This new area of research aims to develop more efficient and

robust photocatalysts that can operate under visible light to address energy and environmental challenges. Recently, Gautam et al. synthesized the (Mg, Co, Ni, Cu, Zn)O catalyst, achieving an MB degradation rate constant of 0.0071 min^{-1} [41]. Fu et al. demonstrated that the $(Bi_{0.2}Na_{0.2}Ba_{0.2}K_{0.2}La_{0.2})TiO_3$ high entropy perovskite oxide (HEPO) can effectively degrade Rhodamine B, with degradation rates of 0.00765 min^{-1} under visible light and 0.01905 min^{-1} under UV light [42]. Jia et al. developed $(La_{0.2}Ce_{0.2}Gd_{0.2}Zr_{0.2}Fe_{0.05})O_2$, which achieved 95.4 % tetracycline degradation under visible light irradiation over a 180 min of treatment time [40].

By using a simple and effective empirical predictor developed by some of the authors [43] to predict *a priori* the formation of bixbyite-structured HEOs, in this paper, $(Ce_{0.2}Zr_{0.2}Yb_{0.2}Er_{0.2}Gd_{0.2})_2O_{3+\delta}$ (briefly labeled as "CZYbEG_CAM" in the following) was synthesized via co-precipitation with ammonium carbonate as precipitating agent. The photocatalytic degradation of MB by CZYbEG_CAM under visible light exposure was examined, with a particular focus on the impact of various parameters, such as pH and photocatalyst dosage, on photocatalytic efficiency. The stability of CZYbEG_CAM was evaluated through multiple reuse cycles, and the key reactive oxygen species (ROS) involved in the degradation process were identified by conducting photocatalytic experiments in the presence of scavenger molecules. Additionally, the performance of CZYbEG_CAM in degrading gallic acid (GA) which is a colorless pollutant, with its chemical structure shown in Fig. 1, was evaluated to rule out any potential photosensitization effects caused by MB molecules. It is worth mentioning that the HEO proposed in this work has never been studied as a photocatalyst. Therefore, the main objective of this manuscript is to determine whether this type of HEO can be a promising material in the field of heterogeneous photocatalysis.

2. Materials and methods

2.1. Chemicals

$ZrO(NO_3)_2$ (99,9 %, Carlo Erba, Milan, Italy), $Ce(NO_3)_3 \cdot 6H_2O$, $Yb(NO_3)_3 \cdot 5H_2O$, $Gd(NO_3)_3 \cdot 6H_2O$, and $Er(NO_3)_3 \cdot 5H_2O$ (99,9 %, Sigma Aldrich, Milan, Italy) were used as metal precursors, ammonium carbonate $((NH_4)_2CO_3$, 99,0 %, Fluka-Honeywell, Steinheim, Germany) was used as precipitating agent for the synthesis of CZYbEG_CAM. MB ($C_{16}H_{18}ClN_3S$, 99.95 %, Sigma Aldrich, Milan Italy), hydrochloric acid (HCl, 37 %, Carlo Erba, Milan, Italy), sodium hydroxide (NaOH, pellets anhydrous, $\geq$ 98 %, Sigma Aldrich, Milan, Italy) and gallic acid ($C_7H_6O_5$, powder, 98 %, Thermo Scientific) were used for the photocatalytic tests. All reagents were used as-purchased without further purification.

2.2. Synthesis of HEO photocatalyst

The adopted synthesis procedure for CZYbEG_CAM can be outlined as follows:

1. All rare-earth and zyrconil nitrates were dissolved in deionized water, resulting in a total cation concentration of 0.1 M (meaning
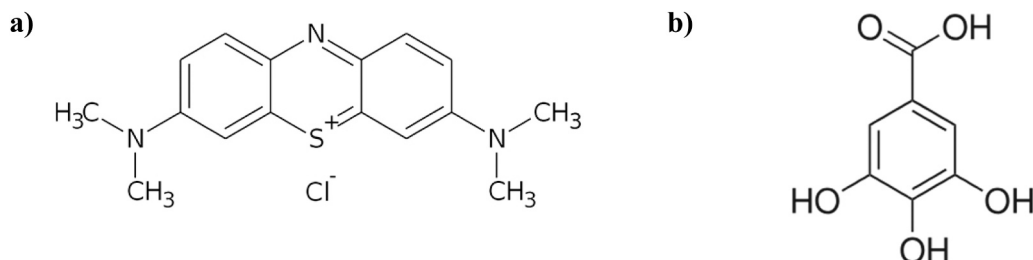

Fig. 1. a) MB; b) GA molecular structure.

each cation concentration was 0.02 M). This solution (referred to as solution A) was stirred vigorously to ensure complete dissolution.

2. The precipitating solution (solution B) was prepared by adding a proper amount of ammonium carbonate to achieve carbonate anions to total cations ratio equal to 10 (R = 10).

3. Solution B was quickly poured into solution A, with mild stirring, resulting in the immediate formation of a pinkish precipitate.

4. The resulting suspension was filtered using a vacuum pump, repeatedly washed with deionized water, and finally dried overnight at 80 °C in static air.

The as-synthesized CZYbEG_CAM powder underwent a calcination step at 750 °C to induce the entropy-driven stabilization of the predicted bixbyite-like phase.

The above-described engineered synthesis route for CZYbEG_CAM derives from a systematic optimization to achieve a single-phase, entropy-stabilized bixbyite structure. First, ammonium carbonate was selected as the best precipitating agent over ammonia and alkaline hydroxides to ensure a more reactive and hard-agglomerate-free as-precipitated precursor. Secondly, the adoption of as-low-as-possible calcination temperature of 750 °C — rather than higher tested temperatures such as 1000 °C, 1250 °C, or 1500 °C — was critical for promoting the entropy-driven stabilization of the target bixbyite-like phase while limiting undesirable particles growth. Definitely, the adopted carefully engineered synthesis conditions grant the obtaining of the entropy-stabilized bixbyite-like structure while maintaining a controlled and submicrometric morphology (characterized by a rather high surface area), needed to favor ensuring enhanced photocatalytic properties.

2.3. Photocatalyst characterization

A structural analysis on both as-prepared and calcined CZYbEG_CAM was carried out via X-ray diffraction with a Panalytical X'PERT MPD diffractometer (Cu Ka radiation).

TG/DTA analysis was performed on the as-precipitated CZYbEG_CAM powder in the air using a heating rate of 10 °C min^{-1} and α-Al$_2$O$_3$ as a reference using a Netzsch Thermoanalyzer STA 409.

CZYbEG_CAM morphology and chemical composition were inspected via Scanning Electron Microscopy (SEM) by using a Philips microscope (XL30) coupled with an electron-dispersive spectroscopy (EDS) probe.

The specific surface area of both as precipitated and calcined powders was determined by measuring the absorption/desorption of liquid nitrogen (Gemini, Micromeritics) after drying at 150 °C and by using the Brunauer, Emmett and Teller (BET) method.

The optical analysis was conducted using a Varian Cary 5000 UV-Vis spectrophotometer equipped with a DR integration sphere (200–600 nm range). The UV-Vis absorption spectrum was plotted using the Kubelka-Munk function (F(R)), while the Tauc method referred to the formula $(F(R)h\nu)^{\gamma} = f(h\nu)$ was used to evaluate the energy gap (E$_g$), the γ factor is equal to 2 or 1/2 for the direct and indirect band gaps, respectively. The photoluminescence (PL) spectrum was collected via a Perkin Elmer Spectrofluorometer LS55. An excitation wavelength (λ_{ex}) of 325 nm was used with 10 nm slits. The PL spectrum was recorded from 350 nm to 650 nm.

To evaluate the ς-potential, the electrophoretic mobility was measured at 25 °C as a function of pH through dynamic light scattering (DLS) with a Zetasizer Nano ZS90 from Malvern Instruments, Worcestershire, UK. Instead, the pH was measured using an XS pH70 Viop from GEASS, Turin, IT. A calcium chloride solution of 1 mM was prepared using ultrapure water (Milli-Q); 0.5 g of the HEO sample was dissolved in 100 mL of the calcium chloride solution and sonicated for 15 min (10 W/mL, 20 kHz) using a DU-65 from Argo Lab, Carpi, IT. The solution's pH was modulated by adding 0.1 M sodium hydroxide to achieve basic pH values or 0.1 M hydrochloric acid for acidic pH values. An integrated confocal micro-Raman system (Invia Micro-Raman,

Renishaw, Wotton-under-Edge, UK) was used to acquire the CZYbEG_CAM Raman spectra. Notch filters are used in the spectrometer to filter out the Rayleigh excitation line. Radiation at 514 nm was used for measurements, with an actual output power of 25 mW. At a magnitude of 20×, the spectra were obtained on the focalized sample.

2.4. Photocatalytic activity test

Photocatalytic tests were performed in a cylindrical pyrex photoreactor (ID = 2.6 cm, L$_{TOT}$ = 41 cm and V$_{TOT}$ = 200 mL). Visible-LEDs strip (nominal power: 10 W; emission in the range 400 – 800 nm; irradiance: 13 mW cm^{-2}) was positioned in contact with the external surface of the photoreactor. The photocatalyst powders (at varying dosages between 0.5 and 3 g L^{-1}) were introduced into 100 mL of an aqueous MB or GA solution at an initial concentration of 10 mg L^{-1} (spontaneous pH). The suspension was kept in the dark for 60 min to allow the adsorption/desorption equilibrium of the dye on the photocatalyst surface to be established. Additionally, the spontaneous pH of the MB solution was adjusted by adding appropriate amounts of hydrochloric acid or sodium hydroxide solutions to evaluate the effect of pH on photocatalytic activity. For analyzing the advancement of the reaction, 3 mL of the solution was periodically collected from the photoreactor and examined using a UV-Vis spectrophotometer (Thermo Scientific Evolution 201). More specifically, the absorbance value at 664 nm [44] to track the MB degradation and the absorbance value at 270 nm for GA degradation were determined during the test time [45]. The extent of pollutant mineralization during irradiation was assessed by monitoring the total organic carbon (TOC) levels in the solutions. Specifically, TOC was quantified by measuring the carbon dioxide generated through high-temperature catalytic oxidation at 680 °C. [46]. The kinetics of photocatalytic pollutant degradation were investigated using the Langmuir-Hinshelwood model [46]. The photodegradation rate (r) can be mathematically represented as:

$$r = \frac{dC}{dt} = \frac{k_r}{1 + K_{ad}} \frac{K_{ad}}{C} \frac{C}{} \tag{1}$$

Where k_r, K_{ad}, and C represent the intrinsic kinetic constant, adsorption equilibrium constant, and contaminant concentration, respectively. The previous equation can be simplified to the first-order kinetics expression with an apparent degradation kinetic constant (k_{app}) since the pollutant concentration is low:

$$-\ln\left(\frac{C}{C_0}\right) = k_r K_{ad} = k_{app} t \tag{2}$$

The slope of -ln (C/C$_0$) vs. time t will provide the apparent degradation kinetic constant value. The following relationships were used to assess both the pollutants (MB and GA) degradation efficiency and the TOC removal (mineralization) at the generic irradiation time t:

$$\textit{Degradation efficiency}(t) = \left(1 - \frac{C(t)}{C_0}\right) * 100 \tag{3}$$

$$\textit{Mineralization efficiency}(t) = \left(1 - \frac{TOC(t)}{TOC_0}\right) * 100 \tag{4}$$

Where $TOC(t)$ is the total organic carbon at the generic irradiation time (mg L^{-1}), TOC_0 is the initial total organic carbon (mg L^{-1}), $C(t)$ is the MB or GA concentration at the generic irradiation time (mg L^{-1}), C_0 is the initial MB or GA concentration (mg L^{-1}).

2.5. Box-Behnken design

In general, the performance of the photocatalytic process depends on different operating parameters. To understand the influences of different operating conditions on the experiment results, the photocatalytic reactions were designed based on an experimental approach through the

use of the most optimal catalyst. Furthermore, an empirical quadratic polynomial model was employed, and all experimental data were collected using a Box-Behnken design. Notably, the Box-Behnken design is a factorial arrangement of at least three parameters utilizing incomplete block designs. In each block, one factor remains constant at the center point, while the others are varied across four distinct combinations within their upper and lower bounds [47]. The experimental design employed a three-level factorial approach, utilizing low (-1), medium (0), and high (+1) levels for each factor. Note that one level was set for each variable (Table 1). The independent variables investigated in this study were solution pH (-), catalyst loading (g L^{-1}), and irradiation duration (min), designated as X1, X2, and X3, respectively. Consequently, a total of 15 experiments were performed.

A polynomial regression model was employed to investigate the causal link between the dependent and independent variables. The equation is reported below (Eq. (5)):

$$R = \beta_0 + \sum_{i=1}^{k} \beta_i \bullet x_i + \sum_{i=1}^{k} \beta_i \bullet x_i^2 + \sum_{i=1}^{k-1} \beta_{ij} \bullet x_i \bullet xj + \varepsilon \qquad (5)$$

Where R is a response variable, β represents a set of regression coefficients (also called constants), k is the number of exogenous variables (independent variables), and $\mathcal{E}$ is an unknown constant error vector. It is crucial to emphasize that a positive sign in the regression equation signifies a synergistic relationship between parameters, whereas a negative sign denotes an antagonistic relationship. The optimal values of the parameters were determined through the estimation of the regression equation and the analysis of the response surfaces visualized by contour plots.

3. Results and discussion

3.1. Structural characterization

Fig. 2a shows the diffraction pattern of the as-precipitated CZYbEG_CAM sample, highlighting the presence of very broad amorphous halos ascribable to the typical short-range order of amorphous ceria-based and zirconia-based precipitates [48].

Conversely, Fig. 2b shows the diffraction pattern of CZYbEG_CAM after calcination and quenching at 750 °C for 1 h. In this case, all the observable peaks are attributable to a bixbyite-like crystal structure (ICDD card n. 00-012-0797), confirming the formation of the designed entropy-stabilized single-phase.

3.2. Thermal behavior

To better understand the nature of the amorphous precursor as well as to analyze the CZYbEG-CAM thermal behavior before the entropy-driven formation of the bixbyite-like phase, a simultaneous differential thermal analysis (DTA) and thermogravimetric analysis (TG) has been carried out on the as-precipitated CZYbEG_CAM.

Fig. 3 shows the DTA-TG curves of CZYbEG_CAM, revealing a rather simple thermal behavior with two different thermal events (α and β), the former located at about 180 °C and the latter (less pronounced) located at about 500 °C, leading to a total weight loss of about 31 %.

Thus, based on both DTA-TG curves and previous results [49], it could be inferred that the as-precipitated CZYbEG_CAM is a hydrated
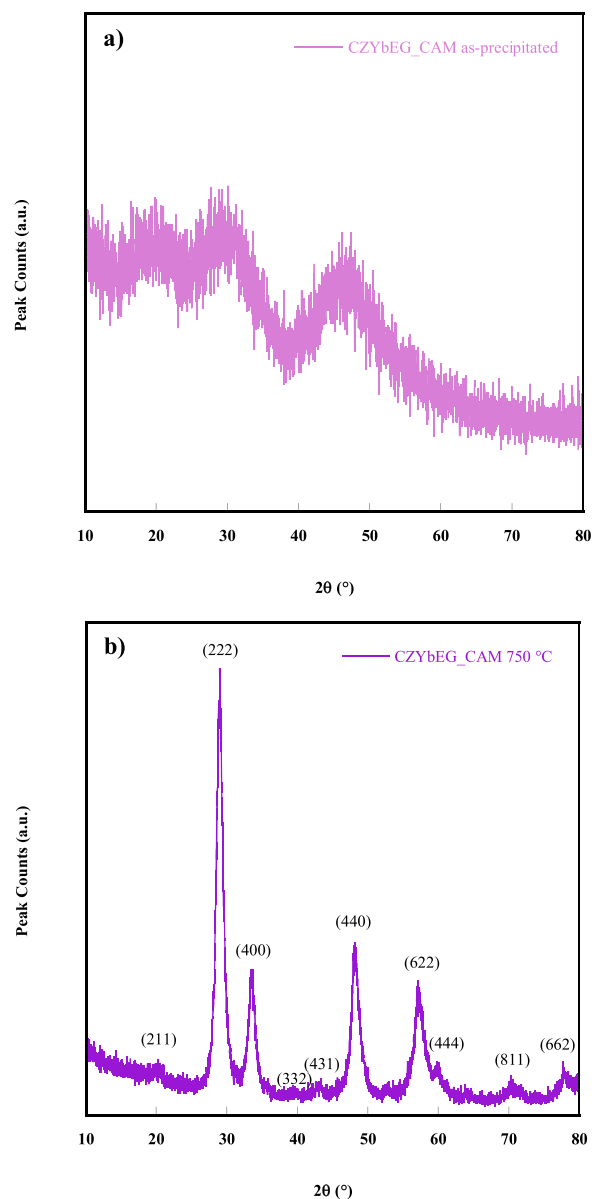

Fig. 2. a) Diffraction pattern of as-precipitated CZYbEG_CAM; b) diffraction pattern of CZYbEG_CAM calcined at 750 °C for 1 h.

(mixed) rare-earth (RE) carbonate with the following chemical formula: $RE_2(CO_3)_3 \cdot 2 H_2O$, exhibiting a theoretical weight loss (considering an "average RE") of about 30 %.

3.3. Microstructural characterization

Fig. 4 shows two exemplary SEM micrographs of both the as-precipitated CZYbEG_CAM (Fig. 4a) and the CZYbEG_CAM calcined at 750 °C for 1 h (Fig. 4b), pointing out similar morphological features (preserved even after calcination, as is usual in the case of rare earth carbonates). In fact, both powders are characterized by softly agglomerated spherical particles, whose average size is nanometric (being smaller than micrometric), this being a common feature in rare-earth-based systems precipitated in carbonate environments [50].

The specific surface area of both the as-precipitated CZYbEG_CAM and the CZYbEG_CAM calcined at 750 °C for 1 h was measured by nitrogen adsorption analysis according to the BET (Brunauer–Emmett–Teller) method, being equal to 61.94 m^2/g for the former and 39.21 m^2/g for the latter. Under the hypothesis that particles are spherical, the

Table 1
Experimental ranges and levels of independent variables.

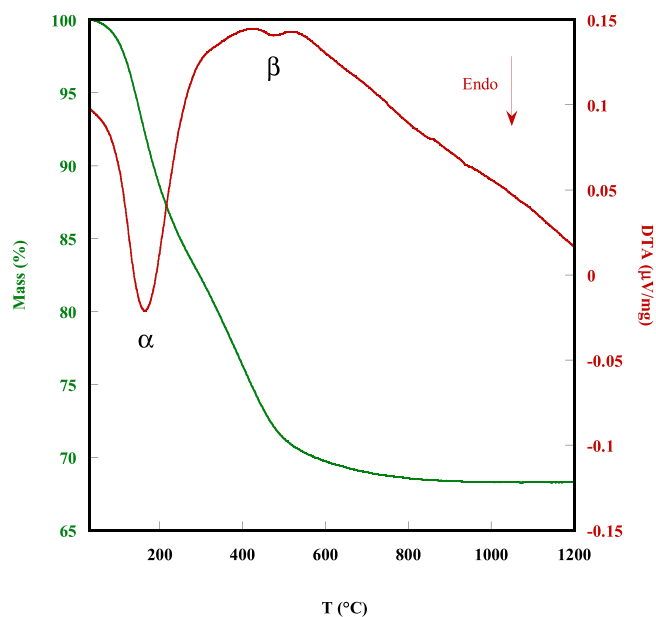| Variables design	Factors	Units	Range and levels		
			-1	0	1
X1	Irradiation time	min	60	120	240
X2	Catalyst amount	g/L	0.5	1	3
X3	pH	-	3.4	11	12

Fig. 3. DTA-TG curves of as precipitated CZYbEG_CAM.

average particle diameter, d_{BET}, can be estimated as follows: $d_{BET} = 6/\rho S$, where ρ is the density and S is the specific surface area derived from BET measurement. Thus, by considering a reference density $\rho = 7.62$ g/cm^3 (for bixbyite-structured Gd_2O_3 from ICDD card n. 00–012–0797), we estimated the average particle diameter as about 13 nm for the as-precipitated CZYbEG_CAM and about 20 nm for the calcined CZYbEG_CAM.

Finally, Fig. 5 displays the elemental mapping of CZYbEG_CAM calcined at 750 °C for 1 h, highlighting a highly homogeneous distribution of all the involved cations, this being an indirect confirmation of the entropy-driven formation of its bixbyite-like single-phase structure.

3.4. Raman analysis

The Raman spectrum of the calcined CZYbEG_CAM photocatalyst is reported in Fig. 6.

The Raman bands observed at approximately 400 cm^{-1} and 459 cm^{-1}

in the sample are characteristic of vibrational modes within the fluorite or defect fluorite structure commonly associated with doped ceria systems. In detail, the signal at about 400 cm^{-1} band typically corresponds to the F_{2g} symmetric breathing mode of oxygen ions surrounding the cationic lattice [51,52]. The features at about 460 cm^{-1} and 615 cm^{-1} are associated with lattice disorder and oxygen vacancy-related vibrational modes arising from the interaction between dopant ions and the ceria host lattice, as well as the formation of oxygen vacancies to maintain charge neutrality. These structural changes are frequently observed in Raman studies of multi-doped ceria and high-entropy oxides [53,54].

The appearance of the high-frequency band in the range 800–1000 cm^{-1} could be attributed to the disordered fluorite structure [55,56].

3.5. UV-Vis and photoluminescence characterization

The UV-Vis absorption spectrum, Fig. SI-1, was analyzed using the Tauc plot method to obtain the direct and indirect energy gap. In Fig. 7, $(F(R)(h\nu)^\gamma$ is plotted as a function of the photon energy, $h\nu$. As suggested by Nundy et al. [57], the application of this method may introduce errors in the evaluation of the band gap (E_g) in multi-component semiconductor systems. In this work, a double tangent approximation was used for a more accurate assessment of Eg values [58]. This correction led to a direct and indirect Eg of 3.7 and 3.2 eV, as reported in Fig. 7a and b, respectively. Making comparisons with literature data is not straightforward due to the variability of HEO systems containing cerium and zirconium. Nundy et al. [57] synthesized five fluorite-type rare earth high-entropy oxides, obtaining Eg values spread over a range of 1.9–3. On the other hand, a low value of Eg, equal to 2.1 was reported by Mariappan Anandkumar et al. [59] for a fluorite high-entropy oxide with chemical formula $(CeGdHfPrZr)O_2$. These values must be carefully evaluated since, as mentioned above, they can be affected by some intrinsic error of the Tauc plot method for these rich cocktails of cations in the oxide structure.

Notably, the inset of Fig. SI-1, focusing on the 400–700 nm range, indicates the presence of intense and narrow absorptions within the visible spectrum, whose wavelengths align with the emission observed in the photoluminescence spectrum (Fig. 8). These absorption bands can be primarily attributed to electronic transitions within the 4f-orbitals of the rare-earth elements [60] (i.e. Er^{3+}, Yb^{3+} and Gd^{3+}). Such features are characteristic of HEOs with fluorite-like structures, which support
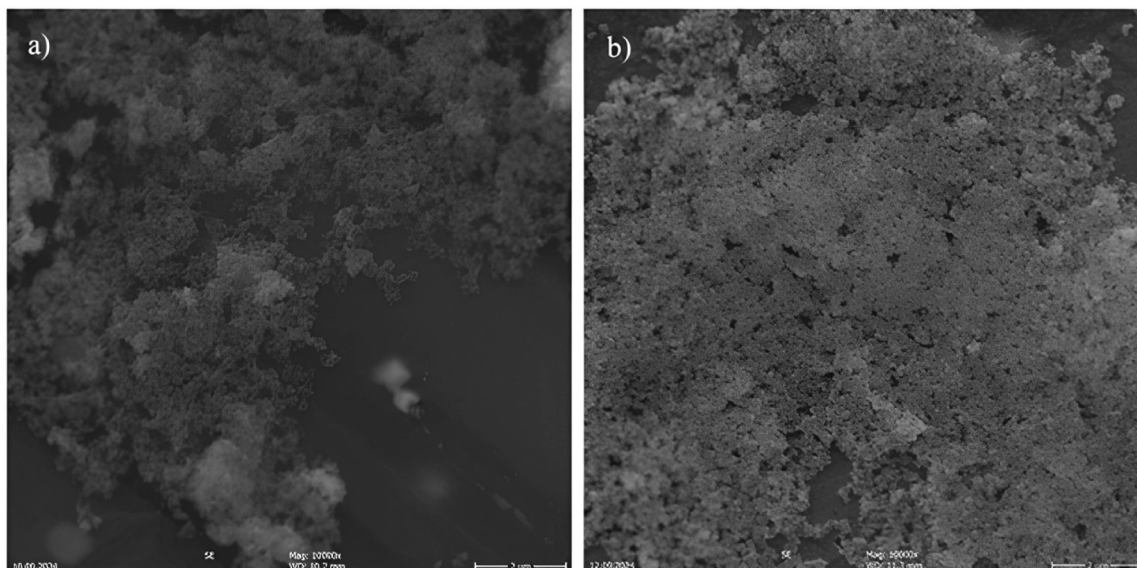

Fig. 4. a) SEM micrograph of the as-precipitated CZYbEG_CAM; b) SEM micrograph of CZYbEG_CAM calcined at 750 °C for 1 h.
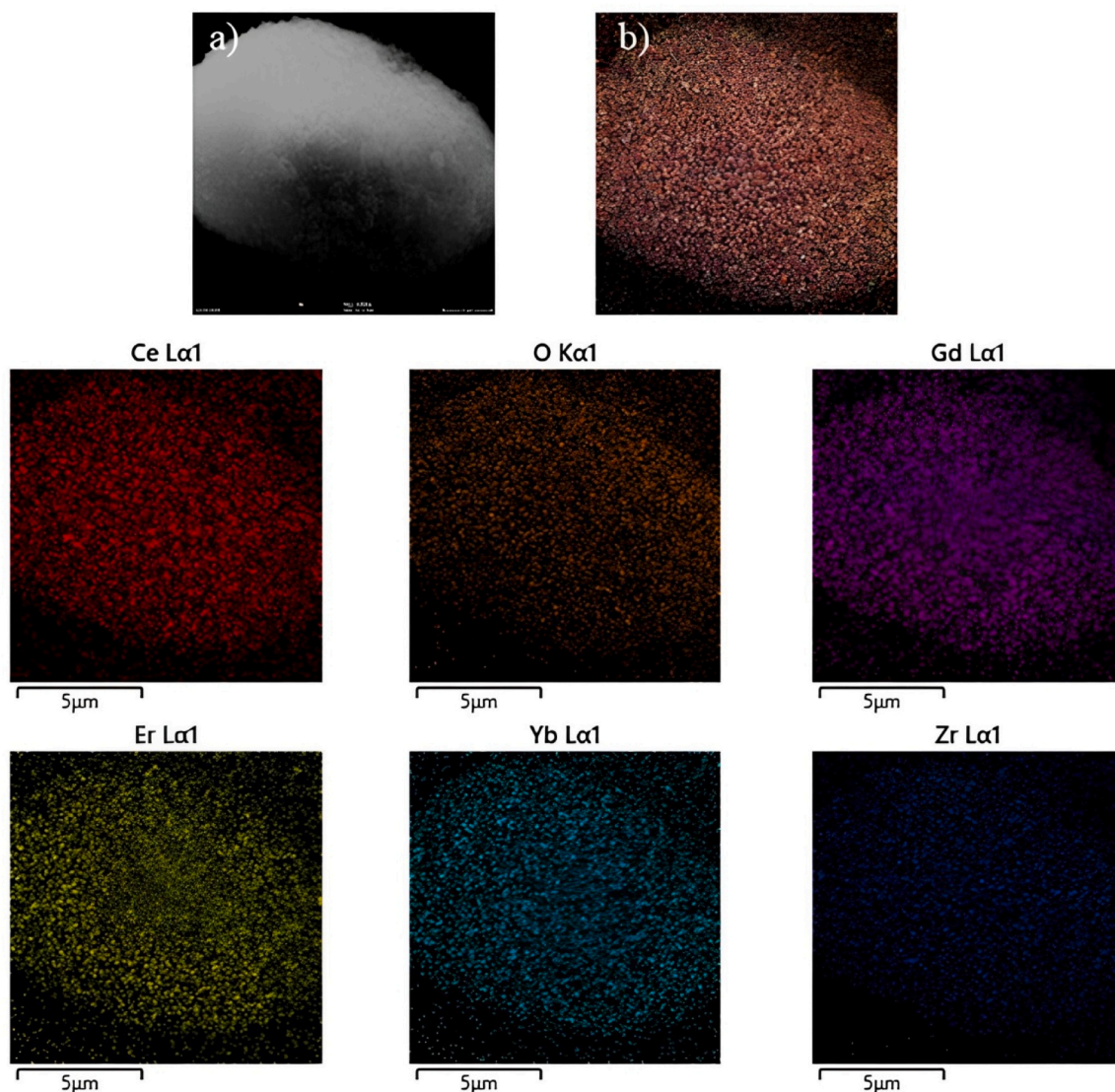
Fig. 5. SEM (a) – EDS (b) mapping of the elemental distribution in CZYbEG_CAM calcined at 750 °C for 1 h.
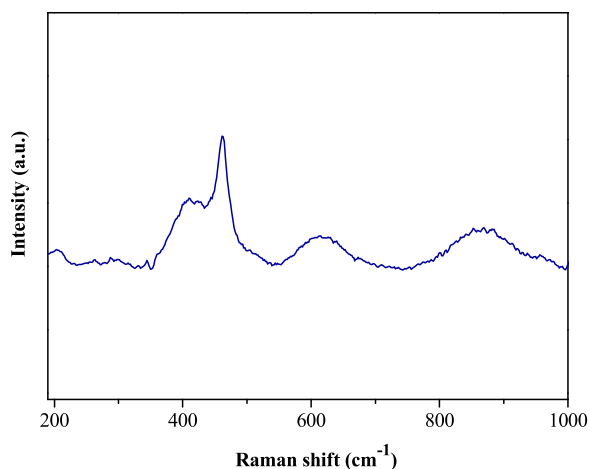

Fig. 6. Raman spectrum of CZYbEG_CAM sample.

the stabilization of multi-element configurations through configurational entropy [30]. The energy levels introduced by the *4f*-orbitals can act as intermediate states within the band gap, facilitating multi-step photon absorption [61]. These features may account for the visible light activity of CZYbEG_CAM (*vide infra*).

To get insight into the electronic structure of prepared HEO, photoluminescence spectroscopy was performed, Fig. 8. Since the sample under study consists of a combination of five different elements, the attribution of the single emission peaks is somewhat puzzling due to the complex electronic band structure of the HEO system. However, some peaks can be related to characteristic transitions. In detail, the peak at 408 nm can be associated to a CB → VB emission involving Ce^{3+} ions, whose presence in CeO_2 causes a sub-band at 1.3–1.5 eV above O2p VB [62]. Moreover, the 425 nm peak can be related to a violet emission in the visible range, likely due to the transition $F^{++} \rightarrow Ce^{3+}$ $4f^1$. F^0, F^+ and F^{++} refer to the states related to oxygen vacancies, which generally lie below Ce^{4+} $4f^0$ and are involved in emission into the visible. These states contain 2, 1 or 0 electrons, respectively.

The peak at 487 nm shows green-blue emission attributed to the $F^{+*} \rightarrow F^+$ transition, and the 515 nm peak corresponds to green emission resulting from the $F^{0*} \rightarrow F^0$ transition, where F* are empty excited energy states [62]. Finally, the peak at 545 nm is tentatively attributed to contributions from erbium (Er), associated with the $^2H_{11/2} \rightarrow$ $^4I_{15/2}$
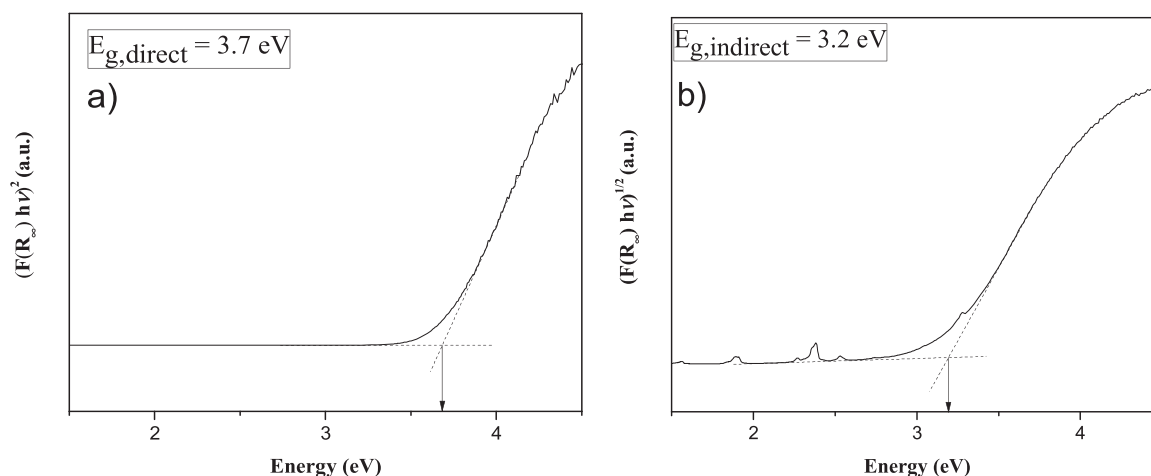
Fig. 7. Tauc plot for (a) direct bandgap calculation and (b) indirect bandgap calculation of CZYbEG_CAM sample based on the F(R) function by Tauc plot relation using the double tangent approximation.
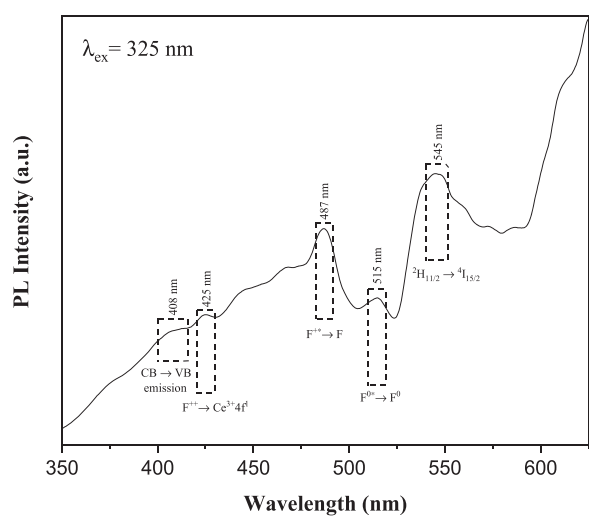

Fig. 8. Photoluminescence spectra of CZYbEG_CAM sample.

transition, emitting in the green region [63]. $^2H_{11/2}$ is an (excited) energy (Stark) level of Er^{3+} $4f^{11}$ electronic configuration and I is the ground-state level of the $4f^{11}$ configuration [64]. Nundy et al.l on a similar system ($Ce_{0.2}Zr_{0.2}La_{0.2}Gd_{0.2}Y_{0.2}O_2$) using an excitation

wavelength of 325 nm obtained a spectrum with numerous sharp peaks [57]. While they did not identify all individual peaks, they attributed all peaks ranging from 450 nm to 600 nm to defect levels originating from oxygen vacancies [57]. Furthermore, defective states can increase non-radiative decay processes, which are therefore not recorded in the PL spectrum [57,62].

4. Photocatalytic activity results

4.1. Photocatalytic degradation results of methylene blue

Fig. 9 displays the photocatalytic MB degradation and mineralization efficiency achieved using 1 g L^{-1} of CZYbEG_CAM sample as a function of irradiation time at the spontaneous pH of MB aqueous solution (pH = 6.8) compared to a test performed without photocatalyst and in the presence of only visible light (photolysis).

The relative concentration of MB and TOC remained unchanged under visible light in the absence of the photocatalyst, confirming that photolysis had a negligible effect [65]. In contrast, the CZYbEG_CAM sample achieved a 30 % MB degradation (Fig. 9a) and a 28 % TOC reduction (Fig. 9b) after 180 min of irradiation. This outcome highlights that CZYbEG_CAM exhibits a certain photocatalytic activity under visible light.
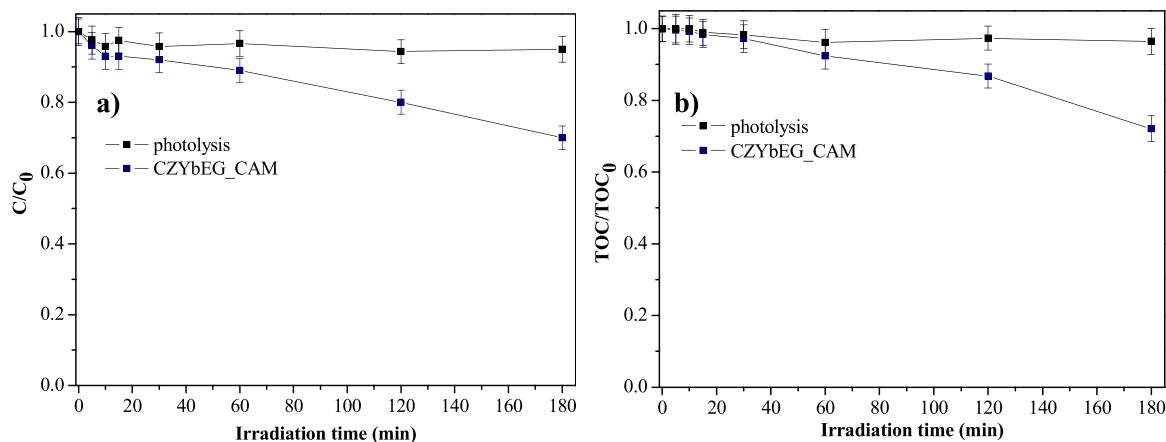

Fig. 9. a) Behaviour of MB relative concentration b) and TOC/TOC$_0$ as a function of irradiation time achieved in the presence of CZYbEG_CAM sample and during the photolysis test.

4.1.1. Influence of pH

The influence of pH was examined to determine whether altering the solution pH could enhance the photocatalytic activity of the CZY-bEG_CAM sample. Specifically, the natural pH of the MB solution, initially at 6.8, was adjusted to 3.4 or 11 by adding 0.1 M aqueous solutions of HCl or NaOH, respectively, to the reaction system.

Fig. 10 illustrates the impact of pH on the degradation and mineralization of MB, both in the dark and under visible light.

The highest dye adsorption on the photocatalytic surface was observed under basic conditions (pH = 11), with an adsorption efficiency of 28 % after 60 min in the dark (Fig. 10a). The MB degradation under visible light was particularly effective at pH = 11, achieving approximately 99 % MB degradation after 180 min of visible light irradiation (Fig. 10a) and the highest degradation kinetic constant of 0.022 min^{-1} (Fig. 10b). In comparison, after the same irradiation time, the MB degradation was much lower, reaching only 26 % and 30 % at pH = 3.4 and 6.8, respectively (Fig. 10a). Additionally, at pH = 11, TOC removal was 44 %, whereas, at the other pH values, TOC removal was significantly lower (Fig. 10b).

In general, changing the pH of the solution can alter the surface charge of the photocatalyst and the ionization level of the pollutant molecules in the solution [66,67]. For this reason, to gain a better understanding of the experimental findings collected at varying MB solution pH values (Fig. 11), the zeta potential (ζ) of the CZYbEG_CAM sample was measured as a function of pH, revealing that the point of zero charge (PZC) of the catalyst was determined to be 8.

Possibly, at pH values lower than the PZC, the photocatalyst surface becomes positively charged as hydroxyl groups on the surface undergo protonation, as reported in the literature [68]. In contrast, at pH values above the PZC, deprotonation of hydroxyl groups dominates, leading to a negatively charged surface [59,68]. Considering the zeta potential trends, the reduced MB adsorption capacity of CZYbEG_CAM at pH values below 7 can be attributed to electrostatic repulsion. At pH = 6.8, MB primarily exists as a cationic species in solution, while at pH = 3.4, a mixture of undissociated and cationic MB species is present [69]. Consequently, at both pH = 6.8 and 3.4, electrostatic repulsion between the positively charged MB species and the CZYbEG_CAM surface hinders the adsorption process. Conversely, under basic conditions (pH = 11), the negatively charged surface of the photocatalyst attracts the positively charged MB molecules, promoting adsorption [69]. Therefore, the photocatalytic performance at pH 11 (pH>pH$_{PZC}$) was superior to that at pH = 6.8 and 3.4 (Fig. 10), highlighting the crucial role of pollutant adsorption in the photocatalytic activity of CZYbEG_CAM [70].
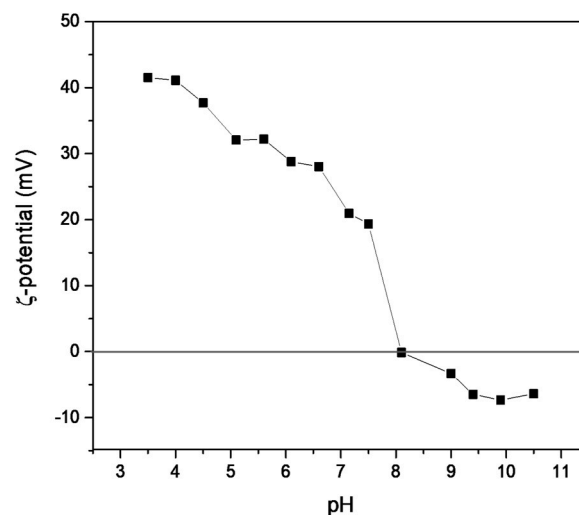

Fig. 11. Point zero charge (PZC) of HEO CZYbEG_CAM photocatalyst.

4.1.2. Influence of CZYbEG_CAM photocatalyst dosage

Photocatalytic experiments were carried out to investigate the impact of different CZYbEG_CAM dosages. The catalyst loading was systematically varied from 0.2 to 3 g/L. Photocatalytic tests were performed using optimized parameters at pH = 11 and with an initial dye concentration of 10 mg/L. Fig. 12 displays the experimental results for dye degradation as a function of irradiation time for varying photocatalyst dosages.

The photocatalytic activity of CZYbEG_CAM enhanced with increasing dosage, ranging from 0.2 to 1 g L^{-1}. A higher photocatalyst dosage provides more active sites for light absorption, leading to accelerated pollutant degradation [71,72]. Specifically, after 180 min of visible light irradiation, the photocatalytic degradation reached approximately 85 % with a photocatalyst dosage of 0.2 g L^{-1} and increased to 99 % with a CZYbEG_CAM dosage of 1 g L^{-1}. Nevertheless, further increasing the dosage to 3 g L^{-1} resulted in a slight decrease in photocatalytic activity (~80 % after 180 min). Excessive catalyst dosage can cause turbidity in the solution, leading to a screening effect that hinders light penetration and reduces the active surface area exposed to light [73,74]. Table SI-1 of Supplementary Material lists the values of the apparent degradation kinetic constant, evidencing that the highest value (0.022 min^{-1}) was obtained with 1 g L^{-1} of CZYbEG_CAM dosage.
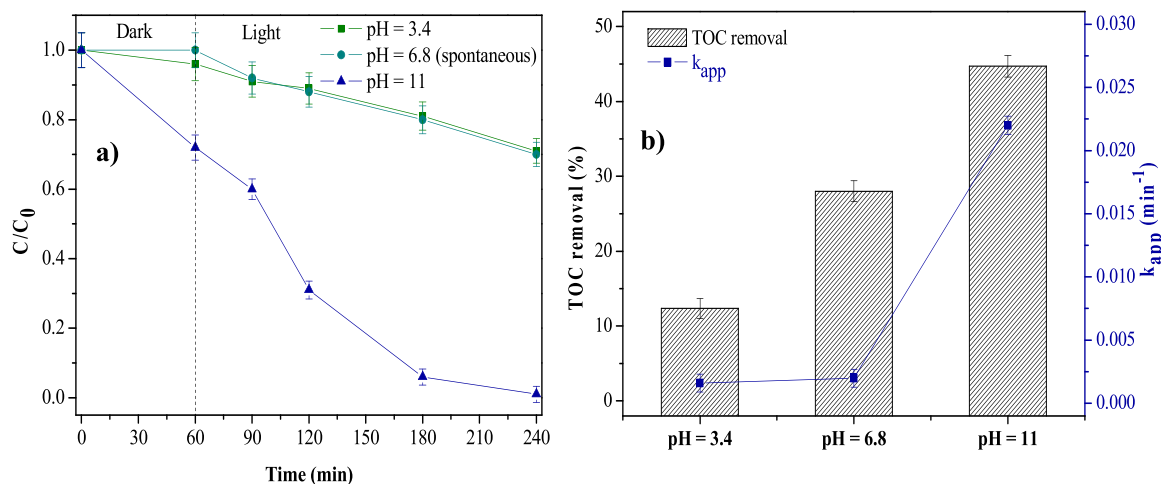

Fig. 10. a) Behaviour of MB relative concentration as a function of test time; b) TOC removal (%) after 180 min of visible light and degradation apparent kinetic constant values obtained by varying the pH.
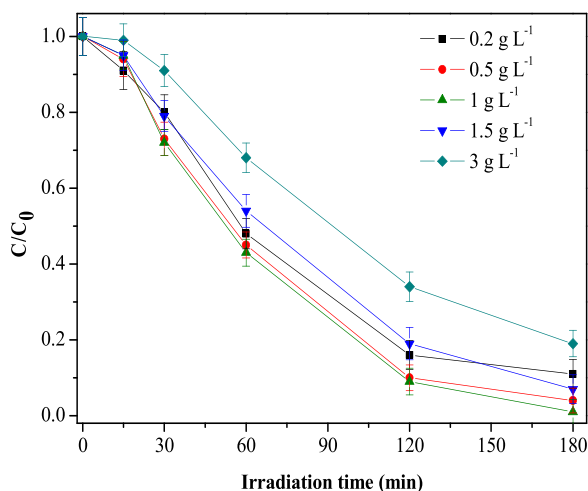
Fig. 12. MB relative concentration as a function of irradiation obtained with CZYBEG_CAM HEO different dosages (pH = 11; initial MB concentration = 10 mg L^{-1}).

4.1.3. Stability tests

Cycling experiments were conducted to evaluate the stability and reusability of the CZYbEG_CAM photocatalyst under optimized conditions (pH = 11; photocatalyst dosage = 1 g L^{-1}). After each cycle, the catalyst was recovered, washed with distilled water and dried at 80°C. The results of these experiments are presented in Fig. 13.

The CZYbEG_CAM exhibited good stability. Specifically, the MB degradation decreased by only approximately 8–9 % with a minor reduction in the apparent kinetic constant from 0.022 min^{-1} to 0.014 min^{-1} after five cycles of reuse (Fig. 13).

The CZYbEG_CAM photocatalyst was recovered after the fifth reuse cycle and analyzed through Raman spectroscopy (Fig. SI-2).

Raman analysis of the spent catalyst demonstrated no appreciable alterations in the spectral signals relative to the fresh photocatalyst, indicating preservation of the fundamental structural framework. In summary, the Raman spectra substantiated the stability and recyclability of the CZYbEG_CAM photocatalyst, in line with the photocatalytic performance observed during the recycling tests (Fig. 13).

4.1.4. Possible photocatalytic reaction mechanism driven by the CZYbEG_CAM photocatalyst

To understand the potential involvement of reactive oxygen species (ROS), including hydroxyl radicals, superoxide, and positive holes, in the photocatalytic MB degradation, CZYbEG_CAM photocatalyst was employed under optimized conditions (photocatalyst dosage= 1 g L^{-1},

pH = 11). In particular, specific scavenger probe molecules were introduced: disodium ethylenediamine tetra-acetate (EDTA, 10 mmol L^{-1}) for trapping positive holes [75], isopropanol (IPA, 10 mmol L^{-1}) for trapping hydroxyl radicals [76], and benzoquinone (BQ, 1 µmol L^{-1}) for trapping superoxide [77].

Fig. 14 shows the influence of EDTA, IPA and BQ on photocatalytic performances.

The addition of scavengers to the aqueous solution influenced the photocatalytic reaction rate. The apparent kinetic constant decreased from 0.022 min^{-1} in the absence of scavengers to 0.015 and 0.014 min^{-1} with the addition of EDTA and IPA, respectively. In contrast, it significantly declined to 0.0077 min^{-1} upon the addition of BQ. From these results, it can be inferred that $\cdot O_2^-$ was the primary ROS responsible for the degradation of the MB dye in compliance with the literature [41,57], although $\cdot$OH and h$^+$ contribute to a lesser extent.

To explain such experimental behavior, the valence band (E_{VB}) and conduction band (E_{CB}) edge potentials at pH = 11 of the CZYbEG_CAM photocatalyst have been estimated using the Mulliken theory through the use of the following equations [59,78]:

$$\chi_j = \frac{1}{2}\left(E_{EAj} + E_{IEj}\right) j = ions\left(Ce^{4+}, Zr^{4+}, Yb^{3+}, Er^{3+}, Gd^{3+}, O^{2-}, \right) \tag{6}$$

$$\chi_{TOT} = \left(\chi_{Ce}^a \times \chi_{Zr}^b \times \chi_{Yb}^c \times \chi_{Er}^d \times \chi_{Gd}^e \times \chi_O^f\right)^{\frac{1}{1+b+c+d+e+f}} \tag{7}$$

$$E_{CB} = \chi - E^e - 0.5 \quad E_g - 0.059pH \tag{8}$$

$$E_{VB} = E_{CB} + E_g \tag{9}$$

Where χ_j is the electronegativity of the j species (ions), E_{EAj} is the electron affinity energy of j species and E_{IEj} is the ionization energy of j species; $a, b, c, d, e,$ correspond to the atomic fraction of ions; χ_{TOT} represents the total electronegativity of the compound (5.44 eV); E_g corresponds to the direct and indirect bandgap of the material estimated from the Tauc plot (3.7 and 3.2 eV respectively), E^e is the energy of free electrons on the hydrogen scale (4.5 eV).

For the indirect band gap scenario, the E_{CB} and E_{VB} were found to be −1.559 V and + 2.141 V vs NHE. In contrast, considering a direct band gap configuration, the E_{CB} and E_{VB} were calculated to be −1.309 V and + 1.891 V vs NHE. Fig. 15 illustrates the possible charge carrier separation and ROS generation in the presence of CZYbEG_CAM photocatalyst, derived from the calculated E_{CB} and E_{VB} values for the two scenarios.

Under light irradiation, electrons (e^-) are excited from the valence band (VB) to the conduction band (CB), generating positive holes (h$^+$) in the VB. The e^- in the CB and h$^+$ in the VB trigger a series of reactions to produce $\cdot O_2^-$ and $\cdot$OH. Specifically, for CZYbEG_CAM as a direct bandgap
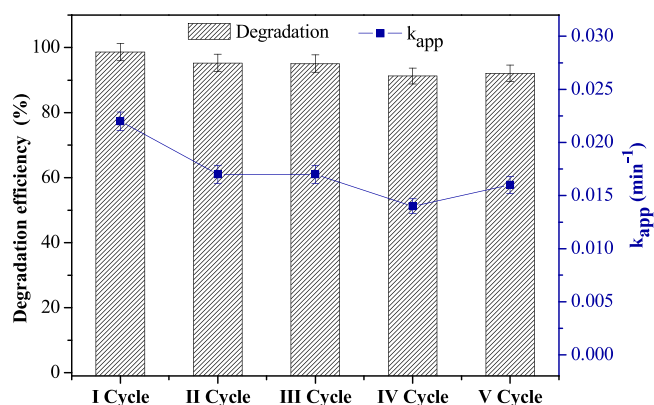

Fig. 13. MB degradation after 180 min of visible light and apparent kinetic constant values in five reuse cycles (pH = 11; initial MB concentration = 10 mg L^{-1}; photocatalyst dosage = 1 g L^{-1}).
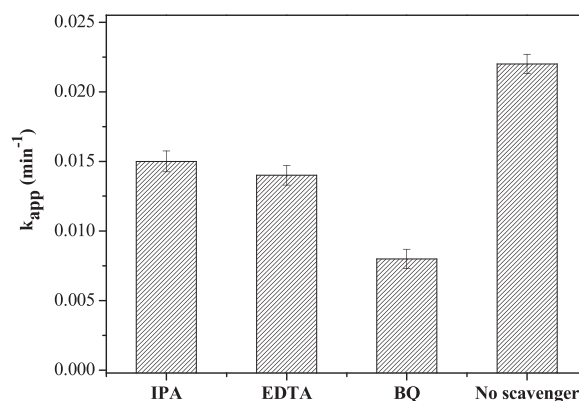

Fig. 14. Apparent kinetic constant of MB degradation for each used scavenger molecule (pH = 11; initial MB concentration = 10 mg L^{-1}; photocatalyst dosage = 1 g L^{-1}).
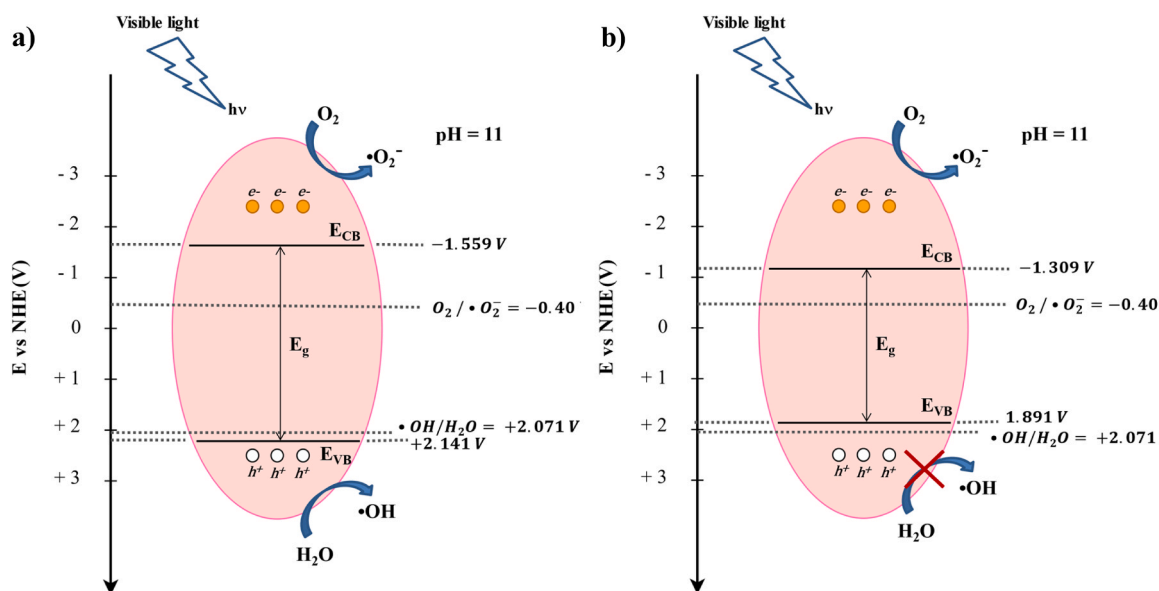
Fig. 15. Schematic diagram of the charge carrier separation and ROS generation in the presence of CZYbEG_CAM photocatalyst considered as (a) direct band gap semiconductor and (b) indirect band gap semiconductor.

semiconductor (Fig. 15a), the excited electrons in the CB can reduce molecular oxygen to ·O$_2^-$. This is possible because the redox potential of the O$_2$/·O$_2^-$ couple (–0.40 V vs NHE at pH = 11) is less negative than the E_{CB} of the photocatalyst (–1.559 V vs NHE at pH = 11). Concurrently, the holes in the VB can oxidize water to ·OH, as the redox potential of the ·OH/H$_2$O pair (+2.071 V vs. NHE at pH = 11) is less positive than the E_{VB} value (+2.141 V vs. NHE at pH = 11).

Conversely, when considering CZYbEG_CAM as an indirect bandgap semiconductor (Fig. 15b), the electrons in the CB still possess the capacity to reduce O$_2$ to ·O$_2^-$, as the redox potential of the O$_2$/·O$_2^-$ pair remains less negative than the E_{CB} (–1.309 V vs NHE at pH = 11). However, due to the redox potential of the ·OH/H$_2$O pair being more positive than the E_{VB} (+1.891 V vs. NHE at pH = 11), the holes in the VB cannot generate ·OH from water.
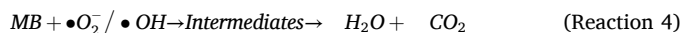
Overall, from a thermodynamic standpoint, the CZYbEG_CAM photocatalyst, in both direct and indirect band gap configurations, can produce ·O$_2^-$ when exposed to light. Conversely, the generation of ·OH is restricted to the direct bandgap configuration of CZYbEG_CAM.

Given that both ·O$_2^-$ and ·OH were identified as reactive species in the photocatalytic degradation of MB, as evidenced by quenching experiments (Fig. 14), we can argue the prepared CZYbEG_CAM operates as a direct band gap semiconductor. This is because, if the photocatalyst were an indirect band gap semiconductor, the photocatalytic reaction rate would not have been affected by the presence of IPA, contrary to the experimental findings depicted in Fig. 14.

Regarding the potential contribution of h$^+$ to the MB photocatalytic degradation mechanism, it's worth considering that MB dye at pH = 11 is present in its cationic form. Therefore, not being an electron donor, the decreased photocatalytic activity after EDTA addition may not indicate direct oxidation of MB by h$^+$ [79]. EDTA traps h$^+$, preventing them from oxidizing water molecules into ·OH. This diminished generation of hydroxyl radicals, in turn, led to a decrease in the observed degradation efficiency of MB (Fig. 14).

By analyzing the experimental results presented in Fig. 14 and considering the band alignment and redox potentials of the ROS

involved, as illustrated in Fig. 15a, a potential simplified mechanism for the photocatalytic degradation of MB by CZYbEG_CAM can be proposed as follows:

$$HEO + h\nu \rightarrow h_{(VB)}^+ + e_{(CB)}^- \qquad \text{(Reaction 1)}$$

$$O_2 + e^- \rightarrow \bullet O_2^- \qquad \text{(Reaction 2)}$$

$$H_2O + h^+ \rightarrow H^+ + \bullet OH \qquad \text{(Reaction 3)}$$

$$MB + \bullet O_2^- / \bullet OH \rightarrow Intermediates \rightarrow H_2O + CO_2 \qquad \text{(Reaction 4)}$$

Upon exposure to visible light, the CZYbEG_CAM photocatalyst activates, exciting electrons from the VB to the CB and leaving behind h$^+$ in the VB (Reaction (1)). The energized electrons in the CB can reduce O$_2$ to ·O$_2^-$ (Reaction (2)). Concurrently, the positive holes in the VB oxidize water molecules to generate ·OH (Reaction (3)). Subsequently, both ·O$_2^-$ and ·OH oxidize the MB dye, forming intermediate compounds that are further oxidized into carbon dioxide and water (Reaction (4)).

Table 2 summarizes the photocatalytic degradation of MB dye by some recently developed HEOs. The data is compared to the performance of the CZYbEG_CAM photocatalyst.

The enhanced photocatalytic activity of the HEO prepared in this work compared to other reported HEOs demonstrates the importance of investigating this class of materials for potential applications in photocatalysis.

4.2. Construction of polynomial expression and 3D response surface for MB photodegradation

The Box–Behnken design matrix for the experimental and predicted values for the MB degradation (%) are regrouped in Table 3.

The maximum degradation observed was 97 % and 97.28 % for experimental and predicted outcomes, respectively. The design model, incorporating three variables and their corresponding responses (R), can be mathematically represented as:

$$R = 0.000924 + 0.2892\ X_1 - 49.6639\ X_2 - 0.0000648 X_3 - 0.00526\ X_1^2 - 0.00112\ X_2^2 - 0.56184\ X_3^2 + 0.432376\ X_1\ X_2 \\ + 1.36693\ X_2\ X_3 + 0.143737\ X_1\ X_3 \qquad (10)$$

Table 2

Comparison of MB photocatalytic degradation with HEO photocatalyst.

HEO	MB initial concentration (mg L^{-1})	Light source	Degradation time (min)	Rate constant (min^{-1})	Refs.
$Ce_{0.2}Gd_{0.2}Hf_{0.2}La_{0.2}Zr_{0.2}O_2$	10	Sunlight	180	0.005	[31]
$Gd_{0.2}Hf_{0.2}La_{0.2}Y_{0.2}Zr_{0.2}O_2$	10	Sunlight	180	0.005	[31]
$(CeGdHfPrZr)O_2$	20	UV	240	0.011	[59]
(Mg, Co, Ni, Cu, Zn)O	10	Visible light	80	0.0071	[41]
$(Ce_{0.2}Zr_{0.2}Yb_{0.2}Er_{0.2}Gd_{0.2})_2O_{3.4}$	10	Visible light		0.022	This work

Table 3

Box-Behnken design matrix with experimental values for independent variables.

Run	Variables			Variables			Experimental Degradation (%)	Predicted Degradation response (%)
	X1	X2	X3	X1	X2	X3		
1	0	1	−1	120	3	3.4	4	3.783494
2	−1	0	0	60	0.5	11	6	5.912365
3	0	−1	−1	120	1	3.4	12	8.645222
4	−1	1	0	60	0.5	11	6	5.912365
5	0	1	1	120	1	12	70	70.81516
6	1	0	−1	240	3	3.4	25	25.43379
7	1	−1	0	240	0.5	11	97	97.28965
8	0	0	0	120	1	11	69	67.85607
9	0	0	0	120	1	11	69	67.85607
10	−1	0	−1	60	0.5	3.4	1	0
11	0	0	0	120	1	11	69	67.85607
12	0	−1	1	120	1	12	70	70.81516
13	−1	−1	0	60	0.5	11	6	5.912365
14	0	0	1	120	1	12	70	70.81516
15	0	1	0	120	3	11	42	42.217

The model strength is assessed using both the R^2 value (0.998) and the adjusted R^2 value (0.997) (Fig. SI-3).

Both are estimated to be in the range of 0.99. Traditionally, the generally agreed-upon threshold value is at least 0.80. The closer this value approaches unity, the more appropriate the model becomes [80]. Finally, three-dimensional response surface plots are drawn in Fig. 16 to visualize the interaction effects between the independent variables and the responses.

It is crucial to emphasize that the derived mathematical expression (Eq. (10)) exclusively characterizes the photocatalytic degradation of MB under the specified experimental parameters. This equation may not apply to other pollutants or under altered experimental conditions [81].
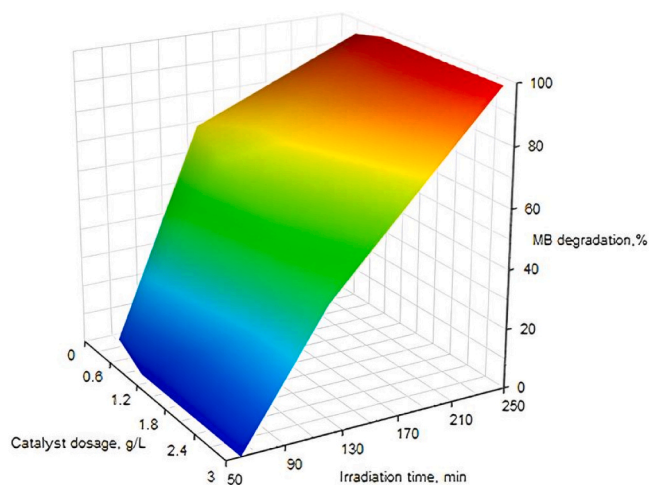

Fig. 16. Response surface showing the effect of catalyst amount (g L^{-1}) and irradiation time (min) on the MB degradation (%) at pH = 11.

4.3. Photocatalytic degradation results of gallic acid

The photocatalytic performance of CZYbEG_CAM was also evaluated for the removal of GA, a colorless pollutant. This was done to rule out potential photosensitization effects from MB molecules on the photocatalyst surface and to confirm the crucial role of pollutant adsorption in modulating the photocatalytic activity of CZYbEG_CAM. Visible light-driven experiments were carried out using the identical experimental apparatus employed for the photocatalytic tests for MB degradation. 100 mL of GA solution with an initial concentration of 10 mg L^{-1} was subjected to irradiation in the presence of 0.5 or 1 g L^{-1} of photocatalyst dosage at pH = 4.8 (spontaneous pH of GA aqueous solution). The photocatalytic results of GA degradation at the two tested photocatalyst dosages are reported in Fig. SI-4.

Before visible light irradiation, at a photocatalyst dosage of 1 g L^{-1}, GA was almost entirely adsorbed onto the photocatalyst surface (approximately 99 %). As a result, the GA photocatalytic degradation cannot be appreciated during the irradiation time. The significant adsorption can be explained by the zero point charge of CZYbEG_CAM (pH$_{ZPC}$ = 8), which is higher than the pH of the GA solution (pH = 4.8). The positively charged catalytic surface (Fig. 11) facilitates GA adsorption through electrostatic interaction phenomena [82], as GA is partially deprotonated at pH 4.8 [83]. By reducing the catalyst dosage to 0.5 g L^{-1}, GA adsorption was diminished, and the relative GA concentration gradually decreased under irradiation, achieving nearly complete degradation (Fig. SI-4) after 180 min of visible light irradiation. Furthermore, GA mineralization was investigated, resulting in a TOC removal exceeding 99 %.

5. Conclusions

In this study, a novel bixbyite-structured High Entropy Oxide (HEO), specifically $(Ce_{0.2}Zr_{0.2}Yb_{0.2}Er_{0.2}Gd_{0.2})_2O_{3.4}$ (CZYbEG_CAM), was successfully synthesized with a simple co-precipitation method by using ammonium carbonate as a precipitating agent and tested as a visible light photocatalyst for the degradation of methylene blue (MB) dye.

The designed single-phase bixbyite-structured HEO has been

obtained after calcination and quenching at 750 °C for 1 h, preserving a high surface area and nanometric particle features similar to the as-precipitated sample, as pointed out by SEM micrographs and confirmed by estimation of particles size based on BET results too.

Furthermore, a thorough analysis of the UV-Vis spectrum showed absorptions in the 400–700 nm region, suggesting a possible visible activity. Indeed, multiple emission peaks were recorded in the visible region of the photoluminescence spectrum, indicating a significantly defective structure

The photocatalytic performance of CZYbEG_CAM was evaluated under various operating conditions, including pH levels, catalyst dosage, and irradiation time. The optimized conditions (pH = 11, catalyst dosage of 1 g L^{-1}, and 180 min of irradiation) resulted in MB degradation and mineralization efficiency of approximately 99 and 45 %, respectively, because of the enhanced adsorption of MB on the catalyst surface. The construction of a polynomial expression and a 3D response surface model for MB photodegradation in the presence of CZYbEG_CAM provided additional evidence supporting this feature.

Analysis of the CZYbEG_CAM photocatalyst band alignment scheme, in conjunction with the redox potentials of reactive oxygen species (ROS) and the observed MB photodegradation rates in the presence of ROS scavengers, indicates that CZYbEG_CAM acts as a direct band gap semiconductor. Moreover, the results suggested that both superoxide and hydroxyl radicals contribute to MB degradation under visible light irradiation. Additionally, the catalyst exhibited stability and reusability across multiple cycles, with a minimal decline in photocatalytic performance, showcasing its potential for real environmental remediation applications.

Photocatalytic tests with gallic acid (GA) showed that the HEO was able to completely degrade also a colorless pollutant, demonstrating that the visible light activity of CZYbEG_CAM observed in the tests with MB was not due to sensitization phenomena of its surface by the adsorbed dye. Additionally, the results with GA further confirmed that the photocatalytic performance of CZYbEG_CAM is strongly dependent on the adsorption of the target contaminant onto its surface.

Overall, the $(Ce_{0.2}Zr_{0.2}Yb_{0.2}Er_{0.2}Gd_{0.2})_2O_{3.4}$ demonstrates significant potential for visible-light-driven applications in wastewater treatment. This material exhibits promising efficacy not only in degrading dye pollutants but also in removing colorless organic contaminants. These findings suggest that this photocatalyst could contribute to developing advanced, multifunctional water treatment processes.

CRediT authorship contribution statement

Gianfranco Dell'Agli: Validation, Supervision, Conceptualization. **Andrea Muscatello:** Formal analysis, Data curation. **Viviana Monfreda:** Formal analysis, Data curation. **Luca Spiridigliozzi:** Writing – review & editing, Writing – original draft, Supervision, Conceptualization. **Olga Sacco:** Validation, Software, Investigation. Katia Monzillo: Investigation, Formal analysis, Data curation. **Antonietta Mancuso:** Investigation, Formal analysis, Data curation. **Vincenzo Vaiano:** Writing – review & editing, Writing – original draft, Supervision, Conceptualization. **Serena Esposito:** Writing – review & editing, Writing – original draft, Supervision, Conceptualization.

Declaration of Competing Interest

The authors declare that they have no known competing financial interests or personal relationships that could have appeared to influence the work reported in this paper.

Acknowledgments

Appendix A. Supporting information

Supplementary data associated with this article can be found in the online version at doi:10.1016/j.jallcom.2025.180435.

References

[1] I. Bashir, F.A. Lone, R.A. Bhat, S.A. Mir, Z.A. Dar, S.A. Dar, Concerns and threats of contamination on aquatic ecosystems, Bioremediation Biotechnol.: Sustain. Approaches Pollut. Degrad. (2020) 1–26.

[2] A. Owhonka, E.F. Fubara, O.B. Justice, Wastewater quality-it's impact on the environment and human physiology: a review, Int. J. Adv. Res. Innov. 9 (2021) 43–58.

[3] S. Nandomah, I.K. Tetteh, Potentially toxic elements pose a threat to environmental quality and human health: the Kumasi Abattoir Ghana in perspective, Environ. Chall. 15 (2024) 100904.

[4] J. Marumure, T.T. Simbanegavi, Z. Makuvara, R. Karidzagundi, R. Alufasi, M. Goredema, C. Gufe, N. Chaukura, D. Halabowski, W. Gwenzi, Emerging organic contaminants in drinking water systems: human intake, emerging health risks, and future research directions, Chemosphere 356 (2024) 141699.

[5] B.J. Singh, A. Chakraborty, R. Sehgal, A systematic review of industrial wastewater management: evaluating challenges and enablers, J. Environ. Manag. 348 (2023) 119230.

[6] J. Lin, W. Ye, M. Xie, D.H. Seo, J. Luo, Y. Wan, B. Van der Bruggen, Environmental impacts and remediation of dye-containing wastewater, Nat. Rev. Earth Environ. 4 (2023) 785–803.

[7] B. Lellis, C.Z. Fávaro-Polonio, J.A. Pamphile, J.C. Polonio, Effects of textile dyes on health and the environment and bioremediation potential of living organisms, Biotechnol. Res. Innov. 3 (2019) 275–290.

[8] Q. Liu, Pollution and treatment of dye waste-water, in: IOP Conference Series: Earth and Environmental Science, IOP Publishing, 2020 052001.

[9] R. Dadashi, M. Bahram, K. Farhadi, Z. Asadzadeh, J. Hafezirad, Photodecoration of tungsten oxide nanoparticles onto eggshell as an ultra-fast adsorbent for removal of MB dye pollutant, Sci. Rep. 14 (2024) 14478.

[10] A. Mancuso, A. Gottuso, F. Parrino, R.A. Picca, V. Venditto, O. Sacco, V. Vaiano, Tuning the selectivity of visible light-driven hydroxylation of benzene to phenol by using Cu, Fe and V oxides supported on N-doped TiO$_2$, Green Chem. 25 (2023) 10664–10677.

[11] A. Mancuso, V. Vaiano, P. Antico, O. Sacco, V. Venditto, Photoreactive polymer composite for selective oxidation of benzene to phenol, Catal. Today 413 (2023) 113914.

[12] A.O. Ibhadon, P. Fitzpatrick, Heterogeneous photocatalysis: recent advances and applications, Catalysts 3 (2013) 189–218.

[13] Y.A.E.H. Ali, A. Azzouz, M. Ahrouch, A. Lamaoui, N. Raza, A.A. Lahcen, Molecular imprinting technology for next-generation water treatment via photocatalysis and selective pollutant adsorption, J. Environ. Chem. Eng. 12 (2024) 112768.

[14] M.A. Iqbal, S. Akram, B. Lal, S.U. Hassan, R. Ashraf, G. Kezembayeva, M. Mushtaq, N. Chinibayeva, A. Hosseini-Bandegharaei, Advanced photocatalysis as a viable and sustainable wastewater treatment process: a comprehensive review, Environ. Res. (2024) 118947.

[15] Y. Zhao, Z. Xu, M. Li, L. Zhou, M. Liu, D. Yang, J. Zeng, R. Xie, W. Hu, F. Dong, S defect-rich MoS$_2$ aerogel with hierarchical porous structure: efficient photocatalysis and convenient reuse for removal of organic dyes, Chemosphere 354 (2024) 141649.

[16] P. Calza, M. Minella, L. Demarchis, F. Sordello, C. Minero, Photocatalytic rate dependence on light absorption properties of different TiO$_2$ specimens, Catal. Today 340 (2020) 12–18.

[17] R. Jain, M. Upadhyaya, A. Singh, R.P. Jaiswal, TiO$_2$ nanoparticles synthesized on graphene nanosheets with varied crystallinity for photocatalytic degradation of MB dye, J. Environ. Chem. Eng. 12 (2024) 113881.

[18] V.K. Pal, D. Kumar, A. Gupta, P.P. Neelratan, L. Purohit, A. Singh, V. Singh, S. Lee, Y.K. Mishra, A. Kaushik, Nanocarbons decorated TiO$_2$ as advanced nanocomposite fabric for photocatalytic degradation of methylene blue dye and ciprofloxacin, Diam. Relat. Mater. 148 (2024) 111435.

[19] T.U. Rahman, H. Roy, A.Z. Shoronika, A. Fariha, M. Hasan, M.S. Islam, H. M. Marwani, A. Islam, M.M. Hasan, A.K. Alsukaibi, Sustainable toxic dye removal and degradation from wastewater using novel chitosan-modified TiO$_2$ and ZnO nanocomposites, J. Mol. Liq. 388 (2023) 122764.

[20] J. Gaur, S. Kumar, M. Pal, H. Kaur, K.M. Batoo, J.O. Momoh, Current trends: zinc oxide nanoparticles preparation via chemical and green method for the photocatalytic degradation of various organic dyes, Hybrid. Adv. (2023) 100128.

[21] A. Mancuso, A. Kiani, O. Sacco, M. Lettieri, R. Fittipaldi, V. Vaiano, M.R. Acocella, V. Venditto, Ball–milled TiO2/biochar hybrid system as a heterogeneous photocatalyst for tannery dyes removal in aqueous solution, J. Mol. Liq. 399 (2024) 124357.

[22] I. Guetni, M. Belaiche, C.A. Ferdi, O. Oulhakem, K.B. Alaoui, F. Zaoui, L. Bahije, Novel modified nanophotocatalysts of TiO$_2$ nanoparticles and TiO$_2$/Alginate beads with lanthanides [La, Sm, Y] to degrade the Azo dye Orange G under UV–VIS radiation, Mater. Sci. Semicond. Process. 174 (2024) 108193.

[23] L.R. Buddiga, G.R. Gajula, B. Sailaja, M.P. Ch, Visible light photocatalytic exploit of P/Zr doped TiO$_2$ nano particles for dye degradation of rose Bengal, Appl. Surf. Sci. Adv. 18 (2023) 100492.

[24] R. Sultana, S.I. Liba, M.A. Rahman, N. Yeachin, I.M. Syed, M.A. Bhuiyan, Enhanced photocatalytic activity in RhB dye degradation by Mn and B co-doped mixed phase TiO$_2$ photocatalyst under visible light irradiation, Surf. Interfaces 42 (2023) 103302.

[25] R. Amrollahi, Comparison of photocatalytic activity of Cu/TiO$_2$, Cu/NiO and Cu/ZnO nanocomposites for the degradation of organic dyes, Appl. Catal. O: Open 195 (2024) 207010.

[26] A. Mancuso, O. Sacco, V. Vaiano, D. Sannino, V. Venditto, S. Pragliola, N. Morante, Visible light active Fe-N Codoped TiO$_2$ synthesized through sol gel method: influence of operating conditions on photocatalytic performances, Chem. Eng. Trans. 86 (2021) 565–570.

[27] S. Mottola, A. Mancuso, O. Sacco, I.De Marco, V. Vaiano, Photocatalytic performance assessment of Fe-N co-doped TiO$_2$/β-cyclodextrin hybrid systems prepared by supercritical antisolvent micronization for organic dyes removal, J. Supercrit. Fluids 201 (2023) 106005.

[28] G. Vitiello, L. Clarizia, W. Abdelraheem, S. Esposito, B. Bonelli, N. Ditaranto, A. Vergara, M. Nadagouda, D.D. Dionysiou, R. Andreozzi, Near UV-irradiation of CuO$_x$-impregnated TiO$_2$ providing active species for H$_2$ production through Methanol photoreforming, ChemCatChem 11 (2019) 4314–4326.

[29] J.W. Yeh, S.K. Chen, S.J. Lin, J.Y. Gan, T.S. Chin, T.T. Shun, C.H. Tsau, S.Y. Chang, Nanostructured high-entropy alloys with multiple principal elements: novel alloy design concepts and outcomes, Adv. Eng. Mater. 6 (2004) 299–303.

[30] C.M. Rost, E. Sachet, T. Borman, A. Moballegh, E.C. Dickey, D. Hou, J.L. Jones, S. Curtarolo, J.-P. Maria, Entropy-stabilized oxides, Nat. Commun. 6 (2015) 8485.

[31] M. Anandkumar, A. Lathe, A.M. Palve, A.S. Deshpande, Single-phase Gd$_{0.2}$La$_{0.2}$Ce$_{0.2}$Hf$_{0.2}$Zr$_{0.2}$O$_2$ and Gd$_{0.2}$La$_{0.2}$Y$_{0.2}$Hf$_{0.2}$Zr$_{0.2}$O$_2$ nanoparticles as efficient photocatalysts for the reduction of Cr (VI) and degradation of methylene blue dye, J. Alloy. Compd. 850 (2021) 156716.

[32] J. Dąbrowa, J. Cieślak, M. Zajusz, M. Moździerz, K. Berent, A. Mikuła, A. Stępień, K. Świerczek, Structure and transport properties of the novel (Dy, Er, Gd, Ho, Y) $_3$Fe$_5$O$_{12}$ and (Dy, Gd, Ho, Sm, Y) $_3$Fe$_5$O$_{12}$ high entropy garnets, J. Eur. Ceram. Soc. 41 (2021) 3844–3849.

[33] L. Spiridigliozzi, M. Biesuz, V. Sglavo, G. Dell'Agli, Design, synthesis and formation mechanism of a novel entropy-stabilized perovskite oxide derived from barium cerate/zirconate, J. Eur. Ceram. Soc. 44 (2024) 2223–2232.

[34] L. Spiridigliozzi, G. Dell'Agli, A novel high-entropy rare-earth hydroxycarbonate synthesized via facile hydrothermal synthesis with superior decomposition temperature, Mater. Lett. 372 (2024) 137090.

[35] L. Spiridigliozzi, G. Dell'Agli, S. Esposito, P. Rivolo, S. Grasso, V.M. Sglavo, M. Biesuz, Ultra-fast high-temperature sintering (UHS) of Ce$_{0.2}$Zr$_{0.2}$Y$_{0.2}$Gd$_{0.2}$La$_{0.2}$O$_{2-\delta}$ fluorite-structured entropy-stabilized oxide (F-ESO), Scr. Mater. 214 (2022) 114655.

[36] D. Bérardan, S. Franger, D. Dragoe, A.K. Meena, N. Dragoe, Colossal dielectric constant in high entropy oxides, Phys. Status Solidi (RRL)–Rapid Res. Lett. 10 (2016) 328–333.

[37] L. Xu, H. Wang, L. Su, D. Lu, K. Peng, H. Gao, A new class of high-entropy fluorite oxides with tunable expansion coefficients, low thermal conductivity and exceptional sintering resistance, J. Eur. Ceram. Soc. 41 (2021) 6670–6676.

[38] Z. Jiang, R. Zhang, H. Zhao, J. Wang, L. Jia, Y. Hu, K. Wang, X. Wang, Preparation of (Ga$_{0.2}$Cr$_{0.2}$Mn$_{0.2}$Ni$_{0.2}$Zn$_{0.2}$) $_3$O$_4$ high-entropy oxide with narrow bandgap for photocatalytic CO$_2$ reduction with water vapor, Appl. Surf. Sci. 612 (2023) 155809.

[39] R. Huang, H. Zhao, Z. Chen, High-entropy materials for photocatalysis, Nano Mater. Sci. (2024).

[40] D. Jia, T. Chigan, X. Li, H. Li, P. Yang, Photocatalytic degradation performance for high-entropy oxide (La$_{0.2}$Ce$_{0.2}$Gd$_{0.2}$Zr$_{0.2}$Fe$_x$) O$_2$ enriched with defects, J. Alloy. Compd. 982 (2024) 173808.

[41] A. Gautam, S. Das, M.I. Ahmad, Band gap engineering through calcium addition in (Mg, Co, Ni, Cu, Zn) O high entropy oxide for efficient photocatalysis, Surf. Interfaces 46 (2024) 104054.

[42] H. Fu, S. Li, Y. Lin, X. Wu, T. Lin, C. Zhao, M. Gao, C. Lin, Enhancement of piezo–photocatalytic activity in perovskite (Bi$_{0.2}$Na$_{0.2}$Ba$_{0.2}$K$_{0.2}$La$_{0.2}$)TiO$_3$ oxides via high entropy induced lattice distortion and energy band reconfiguration, Ceram. Int. 50 (2024) 9159–9168.

[43] L. Spiridigliozzi, C. Ferone, R. Cioffi, G. Dell'Agli, Compositional design of single-phase rare-earth based high-entropy oxides (HEOs) by using the cluster-plus-glue atom model, Ceram. Int. 49 (2023) 7662–7669.

[44] F. Utami, D. Rahman, D. Margareta, H. Rahmayanti, R. Munir, E. Sustini, M. Abdullah, TiO$_2$ photocatalytic degradation of methylene blue using simple spray method, in: IOP Conference Series: Materials Science and Engineering, IOP Publishing, 2019 012026.

[45] A.L. Luna, M.A. Valenzuela, C. Colbeau-Justin, P. Vazquez, J.L. Rodriguez, J. R. Avendano, S. Alfaro, S. Tirado, A. Garduno, M. José, Photocatalytic degradation of gallic acid over CuO–TiO$_2$ composites under UV/Vis LEDs irradiation, Appl. Catal. A: Gen. 521 (2016) 140–148.

[46] D. Sannino, N. Morante, O. Sacco, A. Mancuso, L. De Guglielmo, G. Di Capua, N. Femia, V. Vaiano, Visible light-driven degradation of Acid Orange 7 by light modulation techniques, Photochem. Photobiol. Sci. 22 (2023) 185–193.

[47] S.B. Moussa, Box-Behnken design for the optimization of the photocatalytic degradation of methyl orange using gold-platinum bimetallic nanoparticles doped-1D titania, J. Photochem. Photobiol. A: Chem. 447 (2024) 115284.

[48] G. Accardo, G. Dell'Agli, M.C. Mascolo, L. Spiridigliozzi, S.P. Yoon, Controlled coprecipitation of amorphous cerium-based carbonates with suitable morphology as precursors of ceramic electrolytes for IT-SOFCs, Materials 12 (2019) 702.

[49] L. Spiridigliozzi, C. Ferone, R. Cioffi, G. Dell'Agli, New insights in the hydrothermal synthesis of rare-earth carbonates, Materials 12 (2019) 2062.

[50] L. Spiridigliozzi, G. Dell'Agli, A. Marocco, G. Accardo, S. Yoon, H. Ham, D. Frattini, Engineered co-precipitation chemistry with ammonium carbonate for scalable synthesis and sintering of improved Sm$_{0.2}$Ce$_{0.8}$O$_{1.90}$ and Gd$_{0.16}$Pr$_{0.04}$Ce$_{0.8}$O$_{1.90}$ electrolytes for IT-SOFCs, J. Ind. Eng. Chem. 59 (2018) 17–27.

[51] G. Jayakumar, A. Albert Irudayaraj, A.Dhayal Raj, A comprehensive investigation on the properties of nanostructured cerium oxide, Opt. Quantum Electron. 51 (2019) 312.

[52] Id.C. Silva, F.A. Sigoli, I.O. Mazali, Reversible oxygen vacancy generation on pure CeO$_2$ nanorods evaluated by in situ Raman spectroscopy, J. Phys. Chem. C 121 (2017) 12928–12935.

[53] O. Elmutasim, A.G. Hussien, A. Sharan, S. AlKhoori, M.A. Vasiliades, I.M.A. Taha, S. Kim, M. Harfouche, A.-H. Emwas, D.H. Anjum, Evolution of oxygen vacancy sites in ceria-based high-entropy oxides and their role in N2 activation, ACS Appl. Mater. Interfaces 16 (2024) 23038–23053.

[54] C. Cheng, R. Hao, J. Hou, F. Zhang, F. Cheng, Z. Meng, B. Ren, Y. Miao, L. Xin, X. Wang, Preparation and entropy regulation study of low thermal conductivity and high strength (ZrHfCeYLaX)O oxides, J. Eur. Ceram. Soc. 44 (2024) 4772–4781.

[55] L. Xu, L. Su, H. Wang, H. Gao, P. Guo, M. Niu, K. Peng, L. Zhuang, Z. Dai, High-entropy Sm$_2$B$_2$O$_7$ (B= Ti, Zr, Sn, Hf, Y, Yb, Nb, and Ta) oxides with highly disordered B-site cations for ultralow thermal conductivity, J. Mater. Sci. Technol. 119 (2022) 182–189.

[56] L. Xu, L. Su, H. Wang, M. Niu, L. Zhuang, K. Peng, X. Fan, H. Gao, D. Lu, Phase evolution and thermophysical properties of high-entropy RE2 (Y$_{0.2}$Yb$_{0.2}$Nb$_{0.2}$Ta$_{0.2}$Ce$_{0.2}$)$_2$O$_7$ oxides, J. Am. Ceram. Soc. 105 (2022) 5490–5500.

[57] S. Nundy, D. Tatar, J. Kojčinović, H. Ullah, A. Ghosh, T.K. Mallick, R. Meinusch, B. M. Smarsly, A.A. Tahir, I. Djerdj, Bandgap engineering in novel fluorite-type rare earth high-entropy oxides (RE-HEOs) with computational and experimental validation for photocatalytic water splitting applications, Adv. Sustain. Syst. 6 (2022) 2200067.

[58] P. Makuła, M. Pacia, W. Macyk, How to correctly determine the band gap energy of modified semiconductor photocatalysts based on UV–Vis spectra, , ACS Publ. (2018) 6814–6817.

[59] M. Anandkumar, P. Kannan, S. Sudarsan, E. Trofimov, High-entropy oxide (CeGdHfPrZr)O$_2$ nanoparticles as reusable photocatalyst for wastewater remediation, Surf. Interfaces 51 (2024) 104815.

[60] S.K. Sharma, T. Behm, T. Köhler, J. Beyer, R. Gloaguen, J. Heitmann, Library of UV-visible absorption spectra of rare earth orthophosphates, LnPO$_4$ (Ln= La-Lu, except Pm), Crystals 10 (2020) 593.

[61] A. Sarkar, B. Eggert, L. Velasco, X. Mu, J. Lill, K. Ollefs, S.S. Bhattacharya, H. Wende, R. Kruk, R.A. Brand, Role of intermediate 4f states in tuning the band structure of high entropy oxides, APL Mater. 8 (2020).

[62] G. Iervolino, O. Tammaro, M. Fontana, B. Masenelli, A.D. Lamirand, V. Vaiano, S. Esposito, Tailoring sub-5 nm Fe-doped CeO$_2$ nanocrystals within confined spaces to boost photocatalytic hydrogen evolution under visible light, J. Energy Chem. 101 (2025) 263–277.

[63] A.A. Alaulamie, S. Baral, S.C. Johnson, H.H. Richardson, Targeted nanoparticle thermometry: a method to measure local temperature at the nanoscale point where water vapor nucleation occurs, Small 13 (2017) 1601989.

[64] J.B. Gruber, G.W. Burdick, S. Chandra, D.K. Sardar, Analyses of the ultraviolet spectra of Er^{3+} in Er$_2$O$_3$ and Er^{3+} in Y$_2$O$_3$, J. Appl. Phys. 108 (2010).

[65] O. Sacco, M. Matarangolo, V. Vaiano, D. Sannino, Visible light-driven photocatalytic performance of ZnO coupled with Up-conversion phosphors for the removal of methylene blue, CET J. -Chem. Eng. Trans. 73 (2019).

[66] S. Ravikumar, D. Mani, E. Chicardi, R. Sepúlveda, K. Balu, V. Pandiyan, Y.-H. Ahn, Development of highly efficient cost-effective CdS/Ag nanocomposite for removal of azo dyes under UV and solar light, Ceram. Int. 49 (2023) 9551–9559.

[67] Y. Guo, C. Zhou, L. Fang, Z. Liu, W. Li, M. Yang, Effect of pH on the catalytic degradation of rhodamine B by synthesized CDs/g-C$_3$N$_4$/Cu$_x$O composites, ACS Omega 6 (2021) 8119–8130.

[68] Y. Liu, C. Ye, L. Chen, J. Fan, C. Liu, L. Xue, J. Sun, W. Zhang, X. Wang, P. Xiong, High entropy-driven role of oxygen vacancies for water oxidation, Adv. Funct. Mater. 34 (2024) 2314820.

[69] J.J. Salazar-Rabago, R. Leyva-Ramos, J. Rivera-Utrilla, R. Ocampo-Perez, F. J. Cerino-Cordova, Biosorption mechanism of methylene blue from aqueous solution onto white pine (Pinus durangensis) sawdust: effect of operating conditions, Sustain. Environ. Res. 27 (2017) 32–40.

[70] S.A. Mosavi, A. Ghadi, P. Gharbani, A. Mehrizad, Photocatalytic removal of methylene blue using Ag@ CdSe/Zeoilte nanocomposite under visible light irradiation by response surface methodology, Mater. Chem. Phys. 267 (2021) 124696.

[71] K.H. Rahman, A.K. Kar, Influence of catalyst loading on photocatalytic degradation efficiency of CTAB-assisted TiO$_2$ photocatalyst towards methylene blue dye solution, Bull. Mater. Sci. 45 (2022) 18.

[72] A. Hayoune, H. Akkari, V. Vaiano, N. Morante, D. Sannino, F. Madjene, Synthesis and characterisation of novel catalyst Ag-TiO$_2$ loaded on magnetic Algerian halloysite clay (Fe$_3$O$_4$-HKDD3) for the photocatalytic activity of methylene blue dye in an aqueous medium, Int. J. Environ. Anal. Chem. 103 (2023) 7697–7714.

[73] D. Rajamanickam, M. Shanthi, Photocatalytic degradation of an azo dye Sunset Yellow under UV-A light using TiO$_2$/CAC composite catalysts, Spectrochim. Acta Part A: Mol. Biomol. Spectrosc. 128 (2014) 100–108.

[74] P.L. Hariani, M. Said, Salni, N. Aprianti, Y.A.L.R. Naibaho, High efficient photocatalytic degradation of methyl orange dye in an aqueous solution by CoFe$_2$O$_4$-SiO$_2$-TiO$_2$ magnetic catalyst, J. Ecol. Eng. 23 (2021) 118–128.

[75] H. Li, Z. Hu, H. Yu, Photocatalytic degradation of PFOA by hydrangea-like BiOCl with high oxygen vacancies co-mediated under superoxide radicals and holes, J. Environ. Chem. Eng. 11 (2023) 110590.

[76] A. Ahmadian, S. Ahmadi, B. Goharrizi, Roles of reactive species in photocatalysis: effect of scavengers and inorganic ions on dye removal from wastewater, Int. J. Environ. Sci. Technol. 20 (2023) 6433–6448.

[77] A. Mancuso, O. Sacco, V. Vaiano, D. Sannino, S. Pragliola, V. Venditto, N. Morante, Visible light active Fe-Pr co-doped TiO$_2$ for water pollutants degradation, Catal. Today 380 (2021) 93–104.

[78] D.A. Dryer, M.M. Walczak, PH-dependent redox couple: Illustrating the nernst equation using cyclic voltammetry, J. Chem. Educ. 74 (1997) 1195–1197.

[79] A. Houas, H. Lachheb, M. Ksibi, E. Elaloui, C. Guillard, J.-M. Herrmann, Photocatalytic degradation pathway of methylene blue in water, Appl. Catal. B: Environ. 31 (2001) 145–157.

[80] J. Li, M. Jiang, H. Zhou, P. Jin, K.M. Cheung, P.K. Chu, K.W. Yeung, Vanadium dioxide nanocoating induces tumor cell death through mitochondrial electron transport chain interruption, Glob. Chall. 3 (2019) 1800058.

[81] M. Carotenuto, G. Lofrano, A. Siciliano, F. Aliberti, M. Guida, TiO$_2$ photocatalytic degradation of caffeine and ecotoxicological assessment of oxidation by-products, Glob. Nest J. 16 (2014) 463–473.

[82] C. Nichita, A.-B.F. Mikhailef, E. Vasile, I. Stamatin, Silver nanoparticles synthesis. bioreduction with gallic acid and extracts from Cyperus rotundus L, Dig. J. Nanomater. Biostructures 15 (2020) 419–433.

[83] J. Huguenin, S. Ould Saad Hamady, P. Bourson, Monitoring deprotonation of gallic acid by Raman spectroscopy, J. Raman Spectrosc. 46 (2015) 1062–1066.